Nanoscale Res Lett (2009) 4:274–280
DOI 10.1007/s11671-008-9237-y

NANO EXPRESS

Photocatalytic Degradation of Isopropanol Over $PbSnO_3$ Nanostructures Under Visible Light Irradiation

Di Chen · Shuxin Ouyang · Jinhua Ye

Received: 12 November 2008 / Accepted: 17 December 2008 / Published online: 7 January 2009

Abstract Nanostructured $PbSnO_3$ photocatalysts with particulate and tubular morphologies have been synthesized from a simple hydrothermal process. As-prepared samples were characterized by X-ray diffraction, Brunauer–Emmet–Teller surface area, transmission electron microscopy, and diffraction spectroscopy. The photoactivities of the $PbSnO_3$ nanostructures for isopropanol (IPA) degradation under visible light irradiation were investigated systematically, and the results revealed that these nanostructures show much higher photocatalytic properties than bulk $PbSnO_3$ material. The possible growth mechanism of tubular $PbSnO_3$ catalyst was also investigated briefly.

Keywords Nanostructures · Photocatalysts

Introduction

Since the Honda–Fujishima effect was reported in 1972, considerable efforts have been paid to develop semiconductor photocatalysts for water splitting and degradation of organic pollutants in order to solve the urgent energy and environmental issues [1–9]. However, to date, most of the photocatalysts reported only respond to UV light irradiation (<420 nm). For visible light accounts for about 43% of the solar spectrum, the utilization of visible light is more significant than UV light and thus developing visible light-driven photocatalyst is one of the most important and meaningful subjects in this field. The fundamental steps for photocatalytic reaction of oxide semiconductor mainly include the following processes: (i) the generation of photoexited charges in the semiconductor materials, (ii) the separation and migration of the generated charges without recombination, and (iii) the redox reaction on the surface of the semiconductor. The first and second steps are associated with the electronic structures of the oxide semiconductor, while the third step is strongly relevant to the surface properties of the catalyst [10–12].

Generally, the improvement of surface area always contributes to more reaction sites, which is beneficial to the photocatalytic reaction. With particular microstructures, nanomaterials have recently gained much attention to be used as high-performance photocatalysts with enhanced photocatalytic activities. For example, in our previous work, we reported the synthesis of perovskite $SrSnO_3$ nanostructures [13] from a facile hydrothermal method. Compared with the catalyst from the traditional solid state route, nanostructured $SrSnO_3$ catalysts with larger surface areas showed higher photocatalytic activities for water splitting under UV light irradiation. Undoubtedly, the enhanced photocatalytic activities are mainly attributed to the increased surface areas, which are believed to be one of the efficient approaches to enhance the activity of catalysts. From a similar hydrothermal process, we reported here the preparation of a new visible light-responded photocatalyst, $PbSnO_3$ nanostructures including particulate and tubular shapes. Experimental results confirmed that these nanostructures show distinguished photocatalytic oxidation activity upon mineralizing isopropanol (IPA) into CO_2 in the visible light region.

D. Chen · S. Ouyang · J. Ye (✉)
International Center for Materials Nanoarchitectonics (MANA) and Photocatalytic Materials Center (PMC), National Institute for Materials Science (NIMS), 1-2-1 Sengen, Tsukuba, Ibaraki 305-0047, Japan
e-mail: Jinhua.YE@nims.go.jp

D. Chen
e-mail: chen.di@nims.go.jp

Experimental Section

Synthesis of $PbSnO_3$ Nanostructures

For the synthesis of tubular $PbSnO_3$ nanostructures, two same surfactant–water solutions were first prepared by dissolving 0.2 g poly(vinyl pyrrolidone) (PVP) surfactant in 25 mL distilled water, respectively. Then, equivalent amounts of $Pb(AC)_2$ and Na_2SnO_3 (2 mmol) were dissolved in the above surfactant–water solution at room temperature, separately. After stirred for 30 min, the solutions were mixed together and kept stirring for another 30 min, which were then transferred into a Teflon-lined stainless steel autoclave and subsequently heated at 180 °C for 16 h in an oven. After cooling to room temperature, the yellow precipitate was filtered and washed for several times with distilled water and ethanol, respectively, then dried in air at 70 °C. $PbSnO_3$ nanoparticles were also synthesized in this work using a similar process without the use of surfactant PVP. Brief flowcharts illustrating the formation of $PbSnO_3$ nanostructures are shown in Scheme 1.

Synthesis of Bulk $PbSnO_3$ from SSR

To compare the photocatalytic properties, bulk $PbSnO_3$ was also synthesized by selecting optimal experimental parameters including calcinations temperature and time. For the synthesis of $PbSnO_3$ bulk material, we first dissolved equivalent amounts of $Pb(AC)_2$ and Na_2SnO_3 into distilled water under stirring, and then mixed them to obtain the white precursor. Heating the white precursor at 500 °C for 5 h in a quartz tube under Ar flow resulted in yellow powders. In this process, temperature is very important for the formation of yellow powders due to the instability of $PbSnO_3$ at high temperature.

Characterization

The crystal structure of the as-prepared sample was confirmed by the X-ray diffraction pattern (JEOL JDX-3500 Tokyo, Japan). The morphology and size of the sample were characterized by transmission electron microscope (HRTEM, JEM-3000F) equipped with an X-ray dispersive spectrometer (EDS). UV–Vis diffuse reflectance spectra were recorded on a UV/Vis spectrometer (UV-2500, Shimadzu) and were converted from reflection to absorbance by the standard Kubelka–Munk method. The surface area of the sample was measured by the BET method (Shimadsu Gemini Micromeritics).

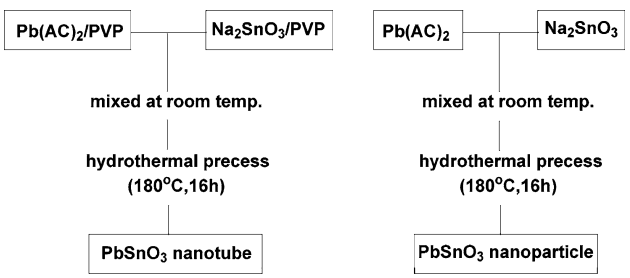

Scheme 1 Flowchart for preparing $PbSnO_3$ nanostructures by the hydrothermal process

Evolution of Photocatalytic Property

The photoactivities of the obtained $PbSnO_3$ nanostructures were evaluated by decomposition of gaseous IPA under visible light irradiation. Typically, 0.1 g $PbSnO_3$ catalyst was spread uniformly in a quartz-made vessel with an irradiation area of 7.8 cm^2. Prior to light irradiation, the vessel was kept in dark for 2 h until an adsorption–desorption equilibrium was finally established. The visible light with light intensity of about 1.8 mW/cm^2 was obtained by using a 300 W Xe lamp with a set of combined filters (L42 + B390 + HA30) and a water filter. The products in the gas phase were analyzed with a gas chromatograph system (GC-14B, Shimadzu, Japan), using a flame ionization detector (FID) for organic compounds determination.

Results and Discussion

Crystal Structure and Morphology

The crystal structure of both as-synthesized $PbSnO_3$ nanostructures from the hydrothermal process and bulk material from the solid-state route were characterized by XRD and the results are shown in Fig. 1. In these patterns, all peaks can be indexed as cubic phase $PbSnO_3$ with pyrochlore-type structure (space group: *Fd3m*). The calculated lattice constant $a = 10.67$ Å is in agreement with previously reported value (JCPDS 17-060). From the XRD patterns, it can be clearly seen that the $PbSnO_3$ nanostructures are of better crystallinity than the bulk material, which might be one of the reasons why nanostructured $PbSnO_3$ show higher photocatalytic activities (detailed contents in the part of discussion). Inset in Fig. 1 is a typical SEM image of the product from the SSR. Scheme 2 shows the crystal structure of pyrochlore-type $PbSnO_3$, an anion-deficient three-dimensional framework consisting of corner-sharing SnO_6 octahedra.

Figure 2a shows a TEM image of as-prepared $PbSnO_3$ nanoparticles from the hydrothermal process. Obviously, the products are consisted of many small nanoparticles with dimensions in the range of 10–15 nm. The corresponding

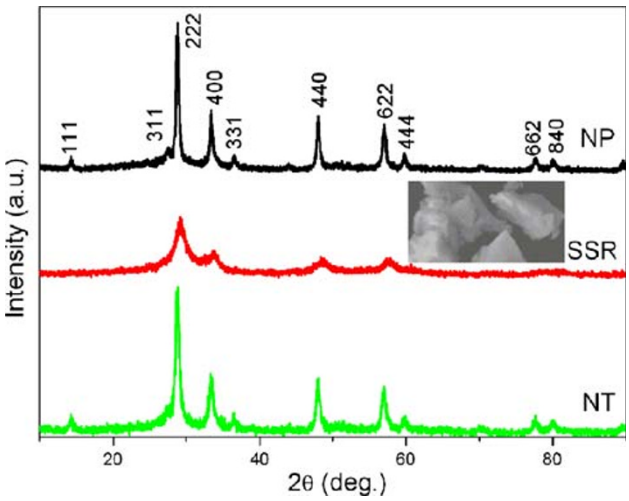

Fig. 1 XRD patterns of the as-prepared $PbSnO_3$ nanostructures from the hydrothermal route and bulk samples from the solid-state route, respectively. Inset shows SEM image of bulk material from SSR

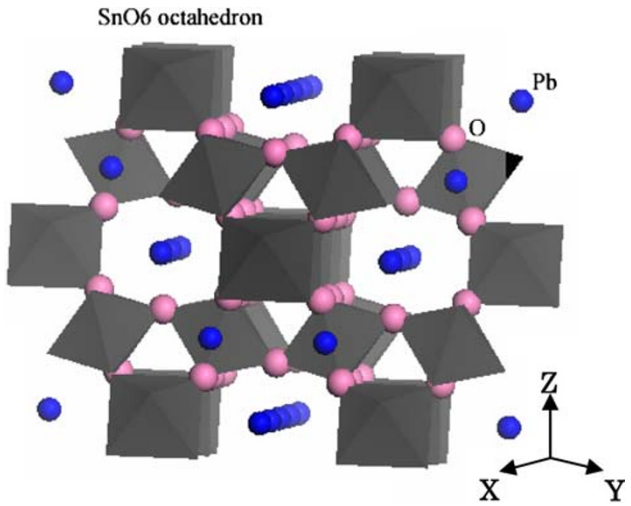

Scheme 2 Crystal structure of pyrochlore $PbSnO_3$

selected-area electron diffraction (SAED) pattern (Fig. 2b) can be readily indexed as cubic phase $PbSnO_3$, which is in agreement with the XRD result. An EDS spectrum in Fig. 2c depicts the presence of Pb, Sn, and O elements, indicating the formation of $PbSnO_3$. In this spectrum, the signals corresponding to Cu arise from the TEM grid. The microstructures of the produced $PbSnO_3$ nanoparticles were investigated using high-resolution TEM. As indicated in Fig. 2d, the nanoparticles are well-crystallized and of good crystallinity. The marked lattice fringes of 0.32 and 0.25 nm correspond well to the (311) and (331) crystalline planes of cubic $PbSnO_3$.

In the presence of surfactant PVP, polycrystalline $PnSnO_3$ nanotubes were obtained instead of nanoparticles. Panels (a) and (b) of Fig. 3 are typical TEM images of as-obtained $PnSnO_3$ nanotubes, which reveal that the nanotubes are polycrystalline with typical diameters of 300–340 nm and wall thickness of 40–80 nm. Figure 3c is the corresponding SAED pattern taken from a single $PbSnO_3$ nanotube, confirming the formation of polycrystalline nanotube. The three polycrystalline rings are in accordance with those of (311), (400), and (533) of cubic phase $PbSnO_3$. Typical HRTEM images of the nanotubes are shown in Fig. 3d and e. It can be seen that the polycrystalline $PbSnO_3$ nanotubes are composed of numerous nanoparticles with diameters of several to ten nanometers. The interplanar spacing was calculated to be about 0.32 nm, corresponding to the (311) plane of cubic $PbSnO_3$, in accordance with the SAED result.

UV–Vis spectra of all three $PbSnO_3$ samples were checked and the spectra are displayed in Fig. 4. It is evident that $PbSnO_3$ nanostructures could absorb much more visible light than bulk sample at the present condition. Corresponding band gaps of $PbSnO_3$ are determined to be 2.8 eV for bulk material, 2.8 eV for nanotubes, and 2.7 eV for nanoparticles from the absorption edges, respectively (as shown in Table 1).

Growth Mechanism

One-dimensional micro- or nanosized tubular materials with hollow interior structure have attracted extraordinary attention owing to their unique properties and potential applications [14–16]. Many kinds of growth mechanisms have been proposed for the formation of nanotubes. For example, the rolling mechanism and template-assisted mechanism have been reported to explain the formation of tubular structure with layered or pseudo-layered structures such as BN [17], $NiCl_2$ [18], Nb_2O_5 [19], Se [20], etc. During the growth of $PbSnO_3$ nanotubes, surfactant PVP was used and was found to be the key issue for nanotube growth. Thus, the surfactant-assisted growth process can be used to explain the formation of these nanotubes. The possible formation process of $PbSnO_3$ nanotubes may involve three following distinctive stages: (i) the generation of $PbSnO_3$ particles, (ii) the adsorption of PVP molecules on the surface of particles and subsequently self-assembly into tubular microstructure, and (iii) the formation of uniform $PbSnO_3$ nanotubes. In the initial stage, cubic $PbSnO_3$ tiny nuclei could easily crystallize and serve as the seeds for the growth of nanotubes. Meanwhile, PVP molecules in the solution would strongly and rapidly adsorb on the surfaces of these nascent nuclei, which confined the crystal growth and efficiently controlled the dimension and morphology of the final products. Then, these particles with high free energy aggregated and self-assembled into tubular structures with the help of PVP template molecules. As a result, the growth of $PbSnO_3$ nanotubes would form eventually by a typical oriented

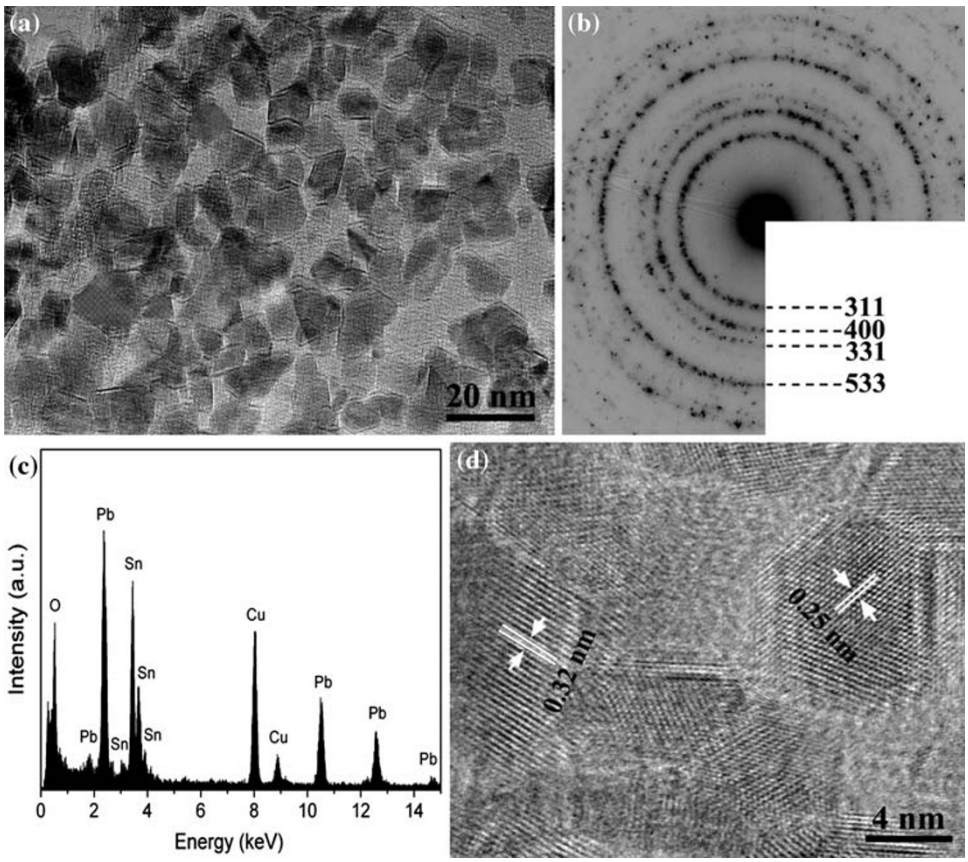

Fig. 2 **a** TEM image; **b** SAED pattern; **c** EDS spectrum; **d** HRTEM image of the as-prepared $PbSnO_3$ nanoparticles from the hydrothermal process

attachment process under the hydrothermal conditions. Meanwhile, the existence of PVP in this solution can alter the surface energies of various crystallographic surfaces to promote selective anisotropic growth of nanocrystals [21].

Photocatalytic Degradation of IPA

The photocatalytic activities of the $PbSnO_3$ nanostructures were evaluated by IPA mineralization under visible light irradiation. Under visible light irradiation, gaseous IPA was gradually oxidized through an acetone intermediate to CO_2, and the concentration changes of IPA, acetone, and CO_2 versus time over $PbSnO_3$ nanoparticles are shown in Fig. 5. It was clear that the concentration of IPA in the reaction system almost decreased from the initial concentration to zero; the concentration of acetone also decreased continually while the concentration of CO_2 increased with the long-term irradiation. Inset in Fig. 5 shows that almost no additional CO_2 gas was detected under dark test, suggesting that degradation of IPA over the catalyst was driven by light irradiation. Figure 6 further displays the concentration changes of evolved acetone over different $PbSnO_3$ nanostructures and bulk material with the increasing of irradiation time. Clearly, acetone was detected over all these catalysts when light was turned on. Among them, particulate $PnSnO_3$ performs the best activity for degradation of IPA under the present conditions.

In this case, the photocatalytic activities for IPA degradation over these catalysts were in the order of nanoparticle > nanotube > bulk material, which was in consistent with that of BET surface areas. As mentioned earlier, BET surface area of catalyst is closely related to its photoactivity. Usually, larger surface area means much more active sites, at which the photocatalytic reaction occurs. Thus, as shown in Table 1, $PbSnO_3$ nanostructures with larger surface areas as 68 m^2/g for nanoparticles and 50 m^2/g for nanotubes, respectively, resulted in enhanced photocatalytic activities than bulk material with 10 m^2/g of surface area. Meanwhile, the improved crystallinity of $PbSnO_3$ nanostructures (shown in XRD patterns) resulted in the increase of photocatalytic activity since it could reduce electron-hole recombination rate.

The wavelength dependence of the rate of acetone evolution from IPA degradation over $PbSnO_3$ nanoparticles was investigated by using different cutoff filters, as shown in Fig. 7. The intensity variation of the incident light with different cutoff filters is given as an inset figure for reference. It is notable that the rate of acetone evolution decreased with increasing cutoff wavelength, which is in good agreement with the UV–Vis diffuse reflectance

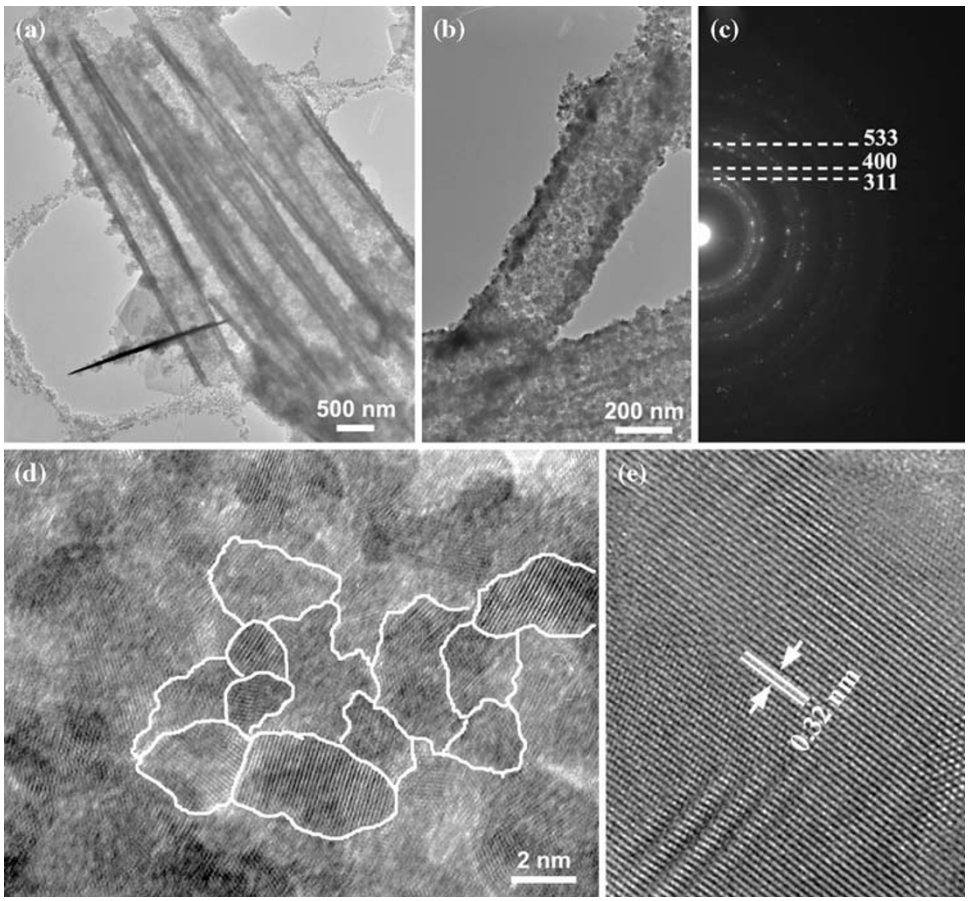

Fig. 3 **a**, **b** TEM images; **c** SAED pattern; **d**, **e** HRTEM images of the as-prepared $PbSnO_3$ nanotubes in the presence of surfactant PVP

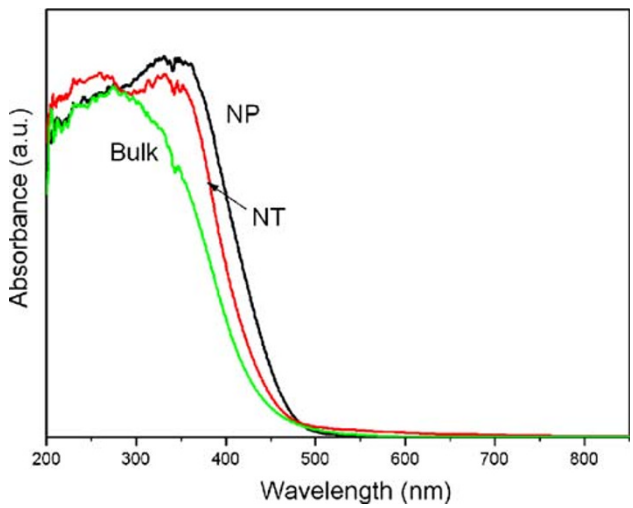

Fig. 4 UV–Vis diffuse reflectance spectra of $PbSnO_3$ nanostructures from the hydrothermal route and $PbSnO_3$ particles from the solid-state route, respectively

spectra of $PbSnO_3$ nanoparticles, indicating the present reaction is driven by a visible light absorption. The used catalysts were again checked by XRD and UV–Vis reflectance spectroscopy to explore the stabilities of

Table 1 Physical and photocatalytic properties of $PbSnO_3$ samples

Sample	Band gap (eV)	BET (m^2/g)	Rate of acetone (ppm/h)
NP	2.7	68	42.2
NT	2.8	50	18.5
Bulk[a]	2.8	10	5.1

[a] Bulk $PbSnO_3$ are prepared from the solid-state route

samples. There was no detectable change between the spectra of $PbSnO_3$ before and after the photodegradation of IPA gas, suggesting that the catalyst was fairly stable for the degradation of organic compounds. For many p-block metal oxides photocatalysts with d^{10} configuration, the VB and CB are the 2p orbital of the oxygen atom and the lowest unoccupied molecular orbital (LUMO) of p-block metal center, respectively [22–24]. Meanwhile, for the lead-containing compounds, it was found that an additional hybridization of the occupied Pb 6s and O 2p orbitals seems to push up the position of the valence band and result in a narrower band gap [25]. Based on the above depiction, we assumed that the VB of $PbSnO_3$ is composed of hybridized Pb 6s and O 2p orbitals, whereas the CB is composed of Sn 5s orbitals, and these bands meet the potential requirements of organic oxidation.

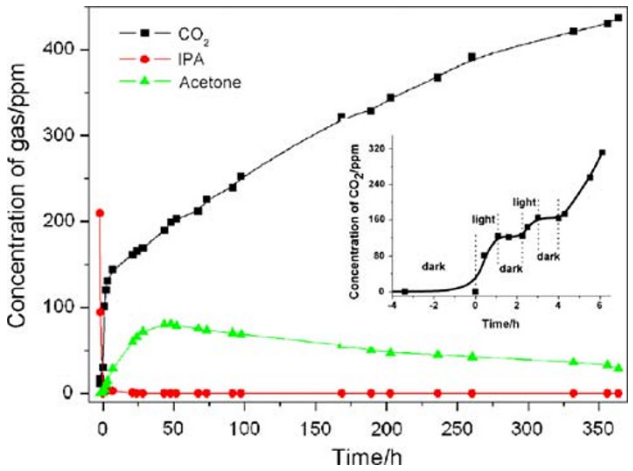

Fig. 5 Changes of IPA, acetone, and CO_2 concentrations as a function of time in the presence of $PbSnO_3$ nanoparticles from the hydrothermal process under visible light irradiation (catalyst: 0.1 g, 300 W Xe lamp, 420 nm cutoff filter and water filter). Inset shows that no CO_2 gas was evolved turning off the light

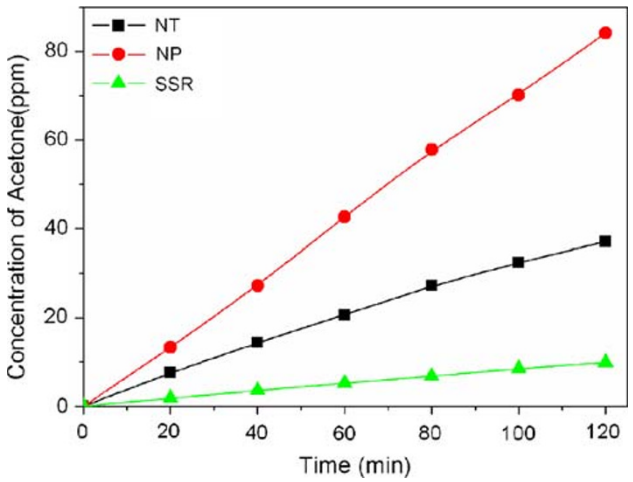

Fig. 6 Acetone evolution from IPA photodegradation over serious $PbSnO_3$ samples (catalyst: 0.1 g, 300 Xe lamp, L42 + B390 + HA30 and water filter)

Conclusion

In summary, we have successfully synthesized pure phase $PbSnO_3$ nanoparticles and nanotubes from the facile hydrothermal process at low temperature. The surfactant PVP used as the capping reagent plays a crucial role in the formation of tubular $PbSnO_3$ structure. $PbSnO_3$ nanostructures with better crystallinity and larger surface areas show enhanced photocatalytic activity for the decomposition of organic pollutant isopropanol under the visible light irradiation than the catalyst prepared by the solid-sate method.

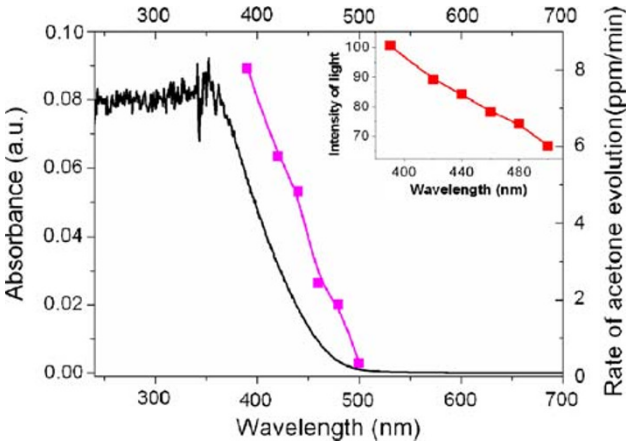

Fig. 7 Wavelength dependence of acetone evolution from isopropanol photodegradation on the cutoff wavelength of incident light, and UV–Vis diffuse reflectance spectrum of $PbSnO_3$ samples. The inset shows the wavelength dependence of light intensity with different cutoff filters (catalyst: 0.1 g, 300 W Xe lamp, 400 nm $< \lambda <$ 500 nm)

Acknowledgment This work was partially supported by the Global Environment Research Fund from the Ministry of Education, Culture, Sports, Science and Technology (MEXT) of the Japanese Government. This work was also supported the World Premier International Research Center Initiative (WPI Initiative) on Materials Nanoarchitectonics, MEXT, Japan and the Strategic International Cooperative Program, Japan Science and Technology Agency (JST).

References

1. A. Fujishima, K. Honda, Nature **238**, 37 (1972). doi:10.1038/238037a0
2. T. Kawai, T. Sakata, Nature **286**, 474 (1980). doi:10.1038/286474a0
3. M.R. Hoffmann, S.T. Martin, W. Choi, Chem. Rev. **95**, 69 (1995). doi:10.1021/cr00033a004
4. C.C. Wong, W. Chu, Environ. Sci. Technol. **37**, 2310 (2003). doi:10.1021/es020898n
5. W. Ho, J. Yu, J. Lin, P. Li, Langmuir **20**, 5865 (2004). doi:10.1021/la049838g
6. M.A. Fox, M.T. Dulay, Chem. Rev. **3**, 341 (1993). doi:10.1021/cr00017a016
7. Z.G. Zou, J.H. Ye, K. Sayama, H. Arakawa, Nature **414**, 625 (2001). doi:10.1038/414625a
8. J. Sato, S. Saito, H. Nishiyama, Y. Inoue, J. Phys. Chem. B **105**, 6061 (2001). doi:10.1021/jp010794j
9. J. Sato, S. Saito, H. Nishiyama, Y. Inoue, J. Photochem. Photobiol. Chem. **148**, 85 (2002). doi:10.1016/S1010-6030(02)00076-X
10. H.B. Fu, C.S. Pan, W.Q. Yao, Y.F. Zhu, J. Phys. Chem. B **109**, 22432 (2005). doi:10.1021/jp052995j
11. H.L. Xu, W.Z. Wang, W. Zhu, J. Phys. Chem. B **110**, 13829 (2006). doi:10.1021/jp061934y
12. J.Q. Yu, A. Kudo, Adv. Funct. Mater. **16**, 2163 (2006). doi:10.1002/adfm.200500799
13. D. Chen, J.H. Ye, Chem. Mater. **19**(18), 4585 (2007). doi:10.1021/cm071321d
14. D.R. Bae, S.J. Lee, S.W. Han, J.M. Lim, D.M. Kang, J.H. Jung, Chem. Mater. **20**, 3809 (2008). doi:10.1021/cm703674d

15. T.W. Ebbesen, P.M. Ajayan, Nature **358**, 220 (1992). doi:10.1038/358220a0
16. B. Chi, E.S. Victorio, T. Jin, Chem. Lett. **35**, 350 (2006). doi:10.1246/cl.2006.350
17. N.G. Chaopra, R.J. Luyken, K. Cherrey, V.H. Crespi, M.L. Cohen, S.G. Louie, A. Zettl, Science **269**, 966 (1995). doi:10.1126/science.269.5226.966
18. Y.R. Hacohen, E. Grunbaum, R. Tenne, J. Sloan, J.L. Hutchison, Nature **295**, 336 (1998). doi:10.1038/26380
19. Y. Kobayashi, H. Hata, M. Salama, T.E. Mallouk, Nano Lett. **7**, 2142 (2007). doi:10.1021/nl0708260
20. Y.R. Ma, L.M. Qi, J.M. Ma, H.M. Cheng, Adv. Mater. **16**, 1023 (2004). doi:10.1002/adma.200400071
21. S.H. Yu, B. Liu, M.S. Mo, J.H. Huang, X.M. Liu, Y.T. Qian, Adv. Funct. Mater. **13**, 639 (2003). doi:10.1002/adfm.200304373
22. J.M. Herrmann, J. Disdier, P. Pichat, J. Catal. **113**, 72 (1988). doi:10.1016/0021-9517(88)90238-2
23. D.S. Muggli, L. Ding, M.J. Odland, Catal. Lett. **78**, 23 (2002). doi:10.1023/A:1014954114655
24. X.Z. Li, F.B. Li, Environ. Sci. Technol. **35**, 2381 (2001). doi:10.1021/es001752w
25. H.G. Kim, O.S. Becker, J.S. Jang, S.M. Ji, P.H. Borse, J.S. Lee, J. Solid State Chem. **179**, 1214 (2006). doi:10.1016/j.jssc.2006.01.024